Applied Catalysis B: Environmental 269 (2020) 118750

Contents lists available at ScienceDirect

Applied Catalysis B: Environmental

journal homepage: www.elsevier.com/locate/apcatb

High-throughput measurement of the influence of pH on hydrogen production from $BaTiO_3/TiO_2$ core/shell photocatalysts

Wenjia Song[a], Eric M. Lopato[b], Stefan Bernhard[b], Paul A. Salvador[a], Gregory S. Rohrer[a,*]

[a] Department of Materials Science and Engineering, Carnegie Mellon University, Pittsburgh, PA 15213, United States
[b] Department of Chemistry, Carnegie Mellon University, Pittsburgh, PA 15213, United States

ARTICLE INFO

Keywords:
Photocatalytic hydrogen generation
pH effect
High-throughput measurement
$BaTiO_3/TiO_2$ core/shell photocatalysts
Surface charge

ABSTRACT

The rates of hydrogen production from four different $BaTiO_3/TiO_2$ core/shell photocatalysts and their components were measured as a function of pH using a parallelized and automated photochemical reactor (PAPCR) to determine the optimized structure and pH condition for photochemical hydrogen production. The amount of hydrogen produced by each reactor in a 96-reactor array was quantified by the color change of a hydrogen-sensitive material. For the core/shell photocatalysts annealed at 600 °C, the increase in hydrogen production rate with pH at pH 3–9 is ascribed to the adsorption of more negatively charged species that bend the bands upward, promoting hole transport to the surface and the oxidation half reaction. At intermediate pH, the core/shell catalyst annealed at 600 °C had the highest reactivity, indicating that the generation and transport of charge carriers were improved by the $BaTiO_3/TiO_2$ core/shell structure. The results demonstrate that PAPCR is an effective way to compare the performance of hydrogen-producing catalysts with different structures and in different operating conditions.

1. Introduction

Currently available photocatalysts do not split water efficiently enough to be commercially competitive for hydrogen production [1]. A variety of modifications have been applied to photocatalysts to accelerate photochemical reactions [2–17]. Most of these modifications have been focused on engineering the catalysts themselves by doping [9–12] or by modifying the surface [8,13–15]. The efficiency of photochemical reactions can also be manipulated by changing the species in aqueous solution. For example, it is simple to tune the pH of the solution, which is effective as long as the catalyst is stable over the pH range [4–7,16,17]. A variation in the adsorption of solution species at the catalyst-solution interface leads to a change in the surface charge and, with it, the shapes of the bands within the catalyst. The shapes of the bands influence the transport of charge carriers to the interface, promoting or suppressing the reaction. The effect of pH on the photochemical reactivity has been studied for relatively simple materials systems, including TiO_2 [16,17], $BaTiO_3$ [4,5], and ZnO [6,7]. However, to the best of our knowledge, the effect of pH on the reactivity of a core/shell catalyst, especially one that has proven to be more efficient than the constituent materials, has not been extensively studied. Computational investigations of TiO_2 coated $BaTiO_3$ indicated that a maximum in reactivity should occur at pH values slightly higher than neutral pH, where the two electrochemical half reactions were balanced [18]. Understanding the effect of pH on a core/shell catalyst will make it possible to control both the catalyst's structure and the solution conditions to improve reactivity.

The spontaneous polarization of ferroelectric $BaTiO_3$ has been used to improve the transport of charge carriers and thus to accelerate photochemical reactions [19,20]. In addition to promoting the transport of charge carriers to the surface, the separation to spatially distinct domains increases the carrier lifetime [21]. Note that $BaTiO_3$ has a bandgap of 3.2 eV [22], so it is a UV light absorbing material. $BaTiO_3$ has been coated with TiO_2 to prevent decomposition [23] and increase the surface area in contact with solution [24]. A previous study of a TiO_2 coated $BaTiO_3$ photocatalyst at a fixed pH showed that maximum reactivity required a synthesis temperature high enough to promote crystallinity and bonding at the $BaTiO_3/TiO_2$ interface, but not so high that the surface area was compromised. Particulate catalysts were also fabricated from similar core/shell structured materials. Visible light absorbing $PbTiO_3/TiO_2$ core/shell catalysts took advantage of the light absorption and ferroelectric polarization of the $PbTiO_3$ core, and the large surface area of the TiO_2 shell [25]. A CdTe/CdS core/shell catalyst combined the extended absorbance region of the core and the chemical stability of the shell [26]. In another catalyst, the charged surface domains of a $BiPO_4$ core or the band potential difference between the

* Corresponding author.
E-mail address: gr20@andrew.cmu.edu (G.S. Rohrer).

https://doi.org/10.1016/j.apcatb.2020.118750
Received 30 November 2019; Received in revised form 14 January 2020; Accepted 10 February 2020
Available online 15 February 2020

C_3N_4 shell and the $BiPO_4$ core promoted the separation and transport of electron-hole pairs at the core-shell interface [27].

The most common way of evaluating the photochemical reactivity of a catalyst is to split water in a gas-tight chamber, extract gas from the reactor headspace at fixed times, and measure the amount of hydrogen via gas chromatography. Most photocatalytic advances have been confirmed by this method; knowing the amount of photogenerated hydrogen and the irradiance of the light source, it is possible to calculate the quantum efficiency [28–30]. While this method has been successfully applied to test the performance of photocatalysts, it would be difficult to scale this procedure for high throughput characterization. The recent development of a colorimetric hydrogen sensitive material has made it possible to construct a highly parallelized and automated photochemical reactor (PAPCR) for a high throughput measurements of hydrogen production [31]. The PAPCR used here consists of 96 small reactors whose headspaces are covered with a hydrogen sensitive material that darkens in proportion to the amount of hydrogen to which it is exposed. When the relation between the amount of hydrogen in the headspace and the appearance of the hydrogen sensitive material is calibrated, optical images of the hydrogen sensitive material can be used to determine the amount of hydrogen produced throughout the reaction by up to 96 different catalysts in a single experiment.

The purpose of this work is to investigate the effect of pH on the photogeneration of hydrogen by $BaTiO_3/TiO_2$ core/shell photocatalysts using a high-throughput method. This $BaTiO_3/TiO_2$ core/shell structure combines the high photochemical efficiency of the ferroelectric core with the high surface area and stability of the shell. The results show that, for the core/shell photocatalysts annealed at 600 °C, the reactivity increases with pH in the pH range 3–9, decreases at pH 9–11, and reaches its maximum at pH 12. For pH 6, the high-throughput experiment reproduces earlier results obtained by conventional hydrogen production experiments [24]. Furthermore, the $BaTiO_3/TiO_2$ core/shell photocatalyst annealed at 600 °C performs better than catalysts annealed at lower and higher temperatures. Taken together, the results show the possibility of accelerating photocatalyst discovery and engineering processes using this high-throughput method.

2. Experimental methods

The method used to synthesize the $BaTiO_3/TiO_2$ core/shell photocatalysts was similar to the process reported previously [32]. Equal weights of micron-sized $BaTiO_3$ (Alfa Aesar) and KCl (Alfa Aesar) were mixed via ball milling with ethanol as the lubricant. The mixture was then stirred for 2 h, before it was dried overnight. The dried mixture was annealed at 1100 °C for 5 h. All annealing processes were carried out in air. Next, the mixture was filtered and washed with boiling deionized (DI) water to remove KCl. The resulting $BaTiO_3$ core particles were dried overnight. Heating the $BaTiO_3$ particles in a molten KCl flux promotes flat surface facets on the particles with relatively fewer defects to support the crystallization of the titania coating. No K or Cl residual was detected in the elemental analysis using energy-dispersive X-ray emission spectroscopy (EDS). Next, the particles were coated with TiO_2 using a previously developed procedure that creates a coating with a thickness that optimizes the reactivity [24]. 1 g of the as-synthesized $BaTiO_3$ cores was suspended in a mixture of 9 ml DI water and 20 ml ethanol. The suspension was stirred for 30 min and a few drops of HCl (Fisher Scientific) was added to the suspension to adjust the pH to ≈ 3. Another solution was prepared by mixing 15 ml ethanol, 8.6 ml titanium(IV) n-butoxide (TBOT, Alfa Aesar), and 1 ml of 2,4-pentanedione (Sigma-Aldrich). This solution was then added to the suspension dropwise while the suspension was being stirred. After the final mixture was stirred for 2 h, it was heated under reflux at ≈ 90 °C for 3 h. The product was collected, washed with ethanol, filtered, and dried overnight before it was annealed at a fixed temperature (500, 600, or 700 °C) for 2 h to crystallize the titania. The powders that were annealed at 500, 600, or 700 °C, after adding the TiO_2 coating, will be referred to as powder types “5”, “6”, or “7”, respectively. The powder referred to as “nB” is made up of nano-size $BaTiO_3$ cores (100 nm, US Research Nanomaterials, Inc.) coated with titania (using the process described above) and annealed at 500 °C. The powder referred to as "s" consists of the nano-size free-standing TiO_2 shell synthesized by the same process and annealed at 500 °C, only without the addition of $BaTiO_3$ cores. The powder referred to as "c" consists of micro-size $BaTiO_3$ cores produced in the KCl flux (uncoated).

To promote hydrogen generation, all of the powders (5, 6, 7, nB, s, and c) were coated with 1 wt.% Pt using an impregnation-reduction method. Powder was added to a H_2PtCl_6 solution (Sigma-Aldrich) and the suspension was stirred for 2 h. The platinum was then reduced using a five-fold excess of $NaBH_4$ (Acros) and NaOH solution (Acros Organics). After the mixture was also stirred for 2 h, the platinized powders were collected by centrifugation, washed with DI water and dried overnight. Prior characterization of Pt added to the surface using a similar technique has shown that they form islands on the surface $5-10$ nm in diameter [33]. Transmission electron microscopy (TEM) images of the $BaTiO_3/TiO_2$ core/shell powder were recorded using 2000EX (JEOL) and are presented in Fig. S1. The results show the expected structure, similar to the previous reports [24,32]. The suspensions used for hydrogen generation were prepared with the six kinds of powders described above, and a mixture of DI water and methanol. The weights of the powders were measured using an analytical balance (Mettler Toledo). The pH of the DI water was adjusted using NaOH or HNO_3 (Fisher Chemical) solutions.

The PAPCR for the high-throughput measurement of photochemical hydrogen generation is illustrated schematically in Fig. 1 and described in more detail in reference [31]. The as-prepared suspensions were injected into 1.1 ml glass shell vials, which were inserted into an array of 96 holes (8 rows by 12 columns) within a metal holder with an open bottom, through which light can be transmitted into the reactors. Next, a hydrogen sensitive film (DetecTape, Midsun Specialty Products) was placed on top of the reactor array. The hydrogen sensitive film reacts to an increase in the local hydrogen concentration by changing its color from light to dark. A quantitative relationship between the color change of the film and the local hydrogen concentration was recently established [31]. The calibration details are described in the Supporting Information and the quantitative relationship is shown in Fig. S2. The response of the tape to H_2 was calibrated in the concentration range of 0–50 % H_2. As illustrated in Fig. S2, the first non-zero point on the calibration curve is at 5 %; when the headspace is 0.7 ml and the total pressure is 1 atm (our most common operating conditions), this corresponds to 2.86 μmol of H_2. We select 5 % as a lower limit for the detection of H_2, although the calibration curve extends to 0 %. To create a

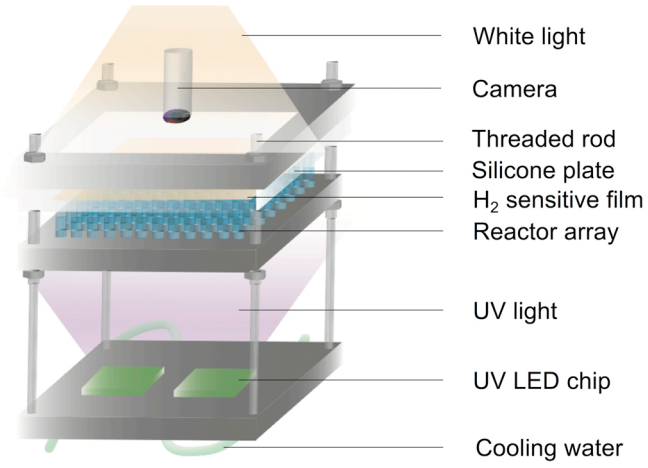

Fig. 1. Schematic illustration of the experimental setup for the high-throughput measurement of photochemical hydrogen generation.

gas-impermeable seal in each vial, a film of fluorinated ethylene propylene (FEP) was placed atop the hydrogen sensitive film. To provide a cushion and ensure uniform sealing across all vials, a layer of 1/16" silicone plate was then added, and the whole system was clamped closed with clear plexiglass pressed down with an aluminum flange structure. Four threaded rods pass through the corners of the plate holding the vials, the silicone sealing plate, and the top plate with the window; the entire assembly is then sealed by tightening nuts on the threaded rods to a uniform pressure using a torque wrench.

Light was provided from below by two 100 W UV LED chips (Chanzon), with a peak wavelength of 380 nm. Note that the position of the chips was adjusted so that the light intensity for all 96 vials was approximately the same. The standard error in maximum hydrogen generation rates due to the vials' different positions relative to the LED chips was 12.3 % measured using 96 identical homogeneous catalyst systems [31]. The UV light source illuminated the reactor array continuously in 6 min intervals. After each 6 min interval, the UV light was turned off, a white light illuminating the hydrogen sensitive film from above was turned on, and a camera recorded an image showing the color of the hydrogen sensitive film that was in contact in the gas in the head space above all 96 reactors. Circulating water was used to cool the LED chips and a fan was used to maintain a constant temperature in the rest of the reactor assembly. The total time of illumination was 6 h, during which 60 images were taken of the hydrogen sensitive film. Eyes should be protected from UV radiation.

The pictures of the hydrogen sensitive film were used to calculate the rate of hydrogen production using the following method. As mentioned above, a relationship between the color of the film and the local hydrogen concentration has been established. In this way, the amount of hydrogen within each vial, at each time interval, can be determined from the contrast in the digital image (up to 50 %). Data from one of the reactors, typical for a catalyst that produces hydrogen, is plotted in Fig. 2. Note that there is an incubation time before hydrogen is detected above 5 % (2.86 μmol, indicated by the dashed blue horizontal line). It is assumed the incubation time arises because enough hydrogen has to be produced to saturate the liquid, first, and to surpass the concentration of 5 % in the headspace of the reactor afterwards. The continuous decrease in the slope at longer times is assumed to be caused by the increase in pressure in the headspace as more hydrogen is produced;

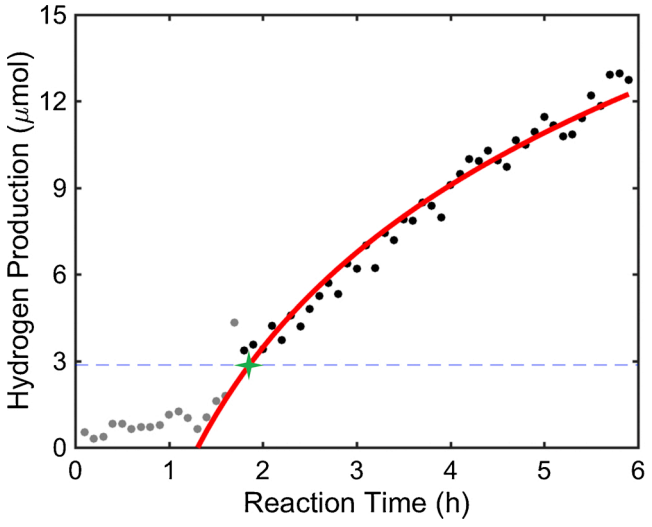

Fig. 2. Plot of the hydrogen production versus reaction time from one of the reactors. The grey circles are data points that were removed from the set for fitting, while the black circles were used in the fitting. The red curve shows the fitted logarithmic function. The blue dashed line represents a hydrogen concentration of 5 %. The green star denotes the position of the intersection of the red curve and the blue line, and the point of maximum slope of the fitted function.

this will be discussed below. After ignoring points below the calibrated limit and an outlier at ~1.7 h (data points colored grey), the rest of the data (plotted with black circles) were fitted to the following logarithmic function:

$$y = a + b\ln x$$

where a and b are fitting parameters. At the intersection of this fitted curve (red solid line) with the lower limit at 5 % H_2 (blue dashed line), indicated by the green star in Fig. 2, the function has its maximum slope, and this slope was assigned to the maximum observable rate of hydrogen production.

The logarithmic fitting was based on the assumption that the reason for the continuous decrease in the rate of hydrogen production was the pressure increase in the headspace with time. The derivation of the logarithmic relationship between the hydrogen production and the reaction time is described in the Supporting Information. Note that previous studies have shown that intermediates including formaldehyde might be the dominant product depending on the reaction time [34]. However, the components of the final product will not influence the logarithmic form of the pressure effect. The justification for modeling the data with the logarithmic function will be discussed further in the following sections.

3. Results

To test reproducibility and the effect of pressure, hydrogen production from the catalysts was measured for 6 h, the reactor was opened and left in a well-ventilated hood for several minutes, and a new hydrogen sensitive film was then placed on the same reactors and the reaction was run again under the same conditions. The results of this second reaction are shown in Fig. 3. These results are essentially the same as the first reaction (see Fig. S3). The circular area above some of the reactors became dark by differing amounts, which is how the film responds to different amounts of hydrogen. The compositions of the suspensions are tabulated in Table 1. The volume of the suspension was 0.4 ml and all vials contained an aqueous solution with 8 vol percent methanol.

Using images taken every 6 min and the pre-established relationship between the local hydrogen concentration and the color of the thin film, we obtained the hydrogen production versus time for each reactor, as shown in Fig. 4. Similar results were found for the first run (see Fig. S4). Note that the incubation period and saturation at long times, already discussed with reference to Fig. 2, are common features of almost all reactors that produced a detectable amount of hydrogen. The reproducibility of these reaction characteristics after venting the headspace is consistent with the model that the reaction rate is controlled by the pressure in the headspace. This model is further supported by the fact that the time dependence of the hydrogen generation fits well to a logarithmic function.

Fig. 5 shows the maximum observable rates of hydrogen production (normalized by dividing by the weight of the powder in the suspension) for the first six rows of the reactors in the array measured in the second run (see Fig. S5 for data from the first run, which is consistent). The type of the powder and the pH of the solution for the suspensions are labeled. An average rate and the standard deviation calculated from five vials filled with identical suspensions are depicted in the color scale bar. The standard deviation is ≈19 % of the average value. The effect of pH on each type of powder is clear by examining each row in Fig. 5. It is obvious that there is a maximum rate at pH 12 for all rows and a local maximum at pH 2–3 for most of the rows. Also, it is clear that only the powder annealed at 600 °C is able to maintain measurable hydrogen yields at all pH values, having another local maximum near pH 9. Assuming the mechanism proposed for the incubation period is correct, then catalysts that produced more hydrogen should have shorter incubation times. The incubation time presented in Fig. S6 is consistent with this proposition.

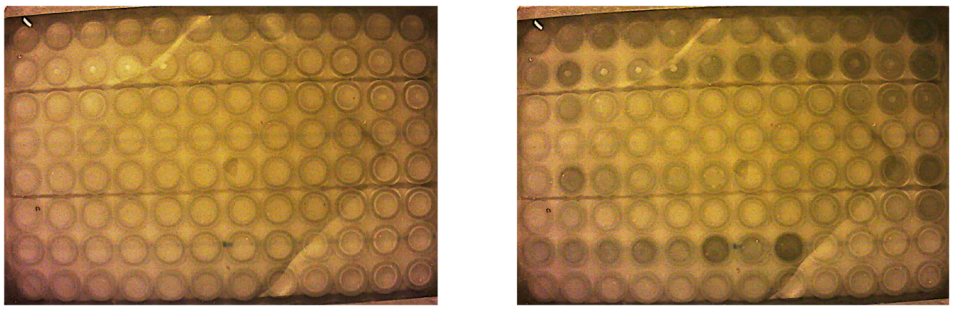

Fig. 3. Images of the reactor array, observed from above, (a) before and (b) after the second 6 h run. The diagonal lines are the results of refraction at the interface between the tape and the silicone plate. The two horizontal lines below the 2nd row and the 5th row are the edges of the hydrogen sensitive film. The film was three rows wide and three of them were used to cover the entire reactor array. The brightness, contrast, and the sharpness of the pictures shown above have been adjusted for better presentation, while the hydrogen yield data was extracted from raw images.

The mass specific rates of hydrogen evolution were previously measured using similar catalysts at pH = 6, but the measurement was carried out by gas chromatography in a conventional reactor system [24]. The comparison between results obtained from these two measurement methods is provided in Fig. S7. The current work is consistent with the previous work, which also found that the core/shell catalysts annealed at 600 °C (6) had the maximum rate of hydrogen production and that the next highest rate was from the high surface area titania (s) without a core. However, the absolute values of the mass specific rates of hydrogen production are not the same. Differences in the reactor systems, illumination sources, and methods of measurement, which will be compared in detail in the discussion section, are responsible for the different measured rates. The parameters *a* and *b* for both runs are shown in Figs. S8 and S9 and the explanations are also provided in the Supporting Information.

Results of powder type “6” and powder type “s” for both the first and the second run were averaged and the data of these two types of powders are compared in Fig. 6. Besides the pH effects described above, it is noted that for powder type “6”, there seems to exist a local maximum at pH 9 and a decrease at pH ≈ 10 before it reaches the maximum at pH 12. However, there appears to be no similar local maximum for powder type “s”.

The influence of the weight of catalyst powder on the absolute (R_{H_2}) and the mass specific ($R_{m,\,H_2}$) rate of hydrogen production is illustrated in Fig. 7. Similar results were obtained for the first run (see Fig. S10). The volumes of the suspensions (0.4 ml), the pH of the solutions (6), and the methanol volume fractions (8 %) were all the same for these five reactors. The absolute rate of hydrogen production increases with the weight of powder. This is reasonable because more catalyst should generate more hydrogen in a fixed time interval. The mass specific rate of hydrogen production shows an opposite trend. In the ideal case, all mass of the powder would contribute equally and the absolute rate would be a linear function of the weight, while the mass specific rate would be constant. The difference between our result and the ideal case indicates that additional catalyst contributes less to making hydrogen, on a per unit mass basis. A possible reason is that the catalyst in the lowest part of the reactor absorbs most of the light and the catalyst added beyond this point is less active because less light reaches it. It could also result from particle aggregation. The aggregation will become increasingly likely as we add more powder, which limits the contact area between the powder and the solution. Even though the 1.6 mg catalyst loading had the highest mass specific rate, most experiments in this work were carried out using a catalyst loading of 3.2 mg, because this quantity could be weighed and handled with less uncertainty.

Fig. 8 shows the effect of the reactor headspace on the mass specific ($R_{m,\,H_2}$) rate of hydrogen production. This set of experiments was conducted separately from the panel described up to this point. The ratio of the weight of the powder to the volume of the solution (8 mg/ ml), the pH of the solution (12), and the methanol volume fraction (8 %) were all the same for these four reactors. It is noted that a larger headspace means a smaller volume of solution, and since the four suspensions have the same weight of powder to volume of solution ratio, reactors with larger headspaces have a smaller total amount of catalyst. Interestingly, the absolute reaction rate did not vary significantly with headspace. The mass specific rates were obtained by dividing the absolute rates by weights and are plotted in Fig. 8. The increase in the mass specific reaction rate with headspace provides further evidence that that increasing pressure in the headspace suppresses hydrogen production because pressure increases more rapidly for smaller headspaces.

The influence of the methanol volume fraction on the mass specific rate of hydrogen production was also investigated. This set of experiments was also conducted separately from the panel described in Table 1. The ratio of the weight of the powder to the volume of the solution (4 mg/ ml), the pH of the solution (6), and the headspace (0.7 ml) were all the same for these four reactors. The rate at 8 % (2.5×10^3 μmol/h/g) is higher than that at 4 % (1.3×10^3 μmol/h/g), but there is no significant change when the methanol volume fraction increases to 12 % (2.3×10^3 μmol/h/g).

4. Discussion

It is noteworthy that the mass specific rate of hydrogen production for the core-shell catalyst annealed at 600 °C is greater than that of the other catalysts throughout much of the pH range. The core-shell photocatalyst is thought to be superior to the unsupported catalyst because band bending within the core helps to separate photogenerated charge

Table 1
Powder type, solution pH, and weight of the powder in each reactor suspension.*

Powder, pH, (Weight of Powder, mg)											
5, 1	5, 2	5, 3	5, 4	5, 5	5, 6	5, 7	5, 8	5, 9	5, 10	5, 11	5, 12
6, 1	6, 2	6, 3	6, 4	6, 5	6, 6	6, 7	6, 8	6, 9	6, 10	6, 11	6, 12
7, 1	7, 2	7, 3	7, 4	7, 5	7, 6	7, 7	7, 8	7, 9	7, 10	7, 11	7, 12
c, 1	c, 2	c, 3	c, 4	c, 5	c, 6	c, 7	c, 8	c, 9	c, 10	c, 11	c, 12
s, 1	s, 2	s, 3	s, 4	s, 5	s, 6	s, 7	s, 8	s, 9	s, 10	s, 11	s, 12
empty	nB, 2	nB, 3	nB, 4	nB, 5	nB, 6	nB, 7	nB, 8	nB, 9	nB, 10	nB, 11	nB, 12
6, 6	6, 6, 1.6	6, 6	6, 6, 6.4	6, 6	6, 6, 12.8	6, 6	6, 6, 25.6	empty	empty	empty	empty
empty	empty	empty	empty	empty	empty	empty	empty	empty	empty	empty	empty

* For those with only two parameters, the weight of powder, 3.2 mg, was omitted.

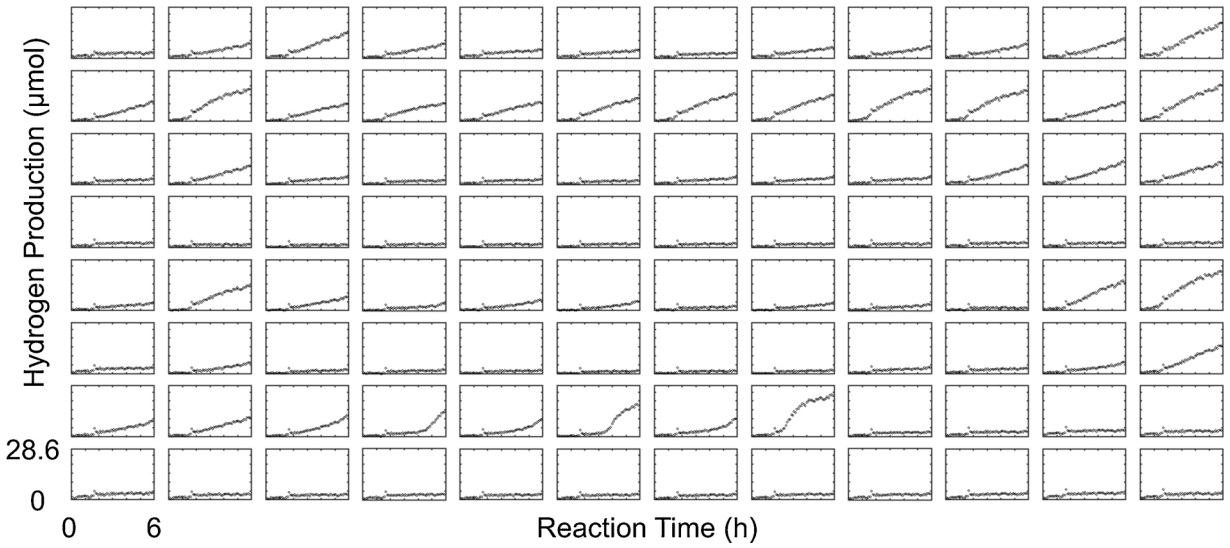

Fig. 4. The hydrogen production as a function of reaction time for each reactor in the array for the second run. The ranges of the x-axis (0 to 6 h) and the y-axis (0 to 28.6 μmol) are the same for all plots.

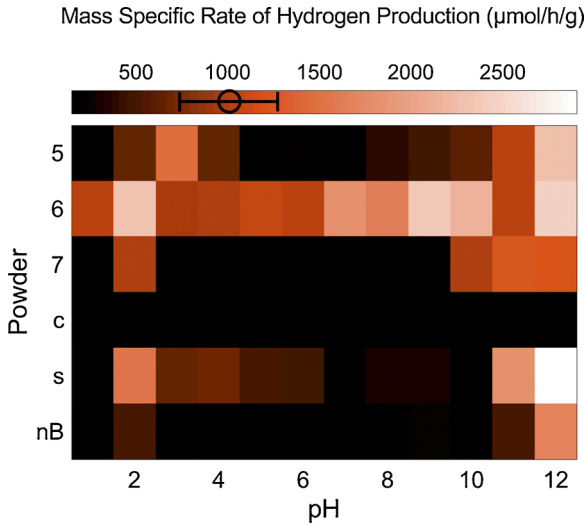

Fig. 5. Mass specific rate of hydrogen production from suspensions with six types of powders under different pH conditions for the second run. The average value and the standard deviation calculated from five vials containing identical suspensions are depicted in the color scale bar. The bar is twice the standard deviation.

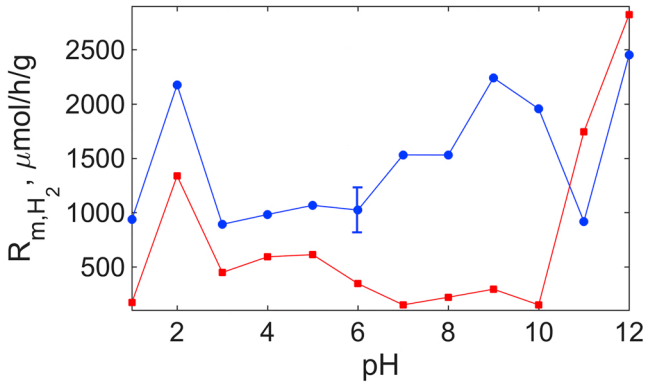

Fig. 6. Mass specific rate of hydrogen production from suspensions with powder type "6" (denoted by blue circles) and powder type "s" (denoted by red squares) under different pH conditions. The values and the standard deviation are average values calculated from the first and the second run. The bar is twice the standard deviation.

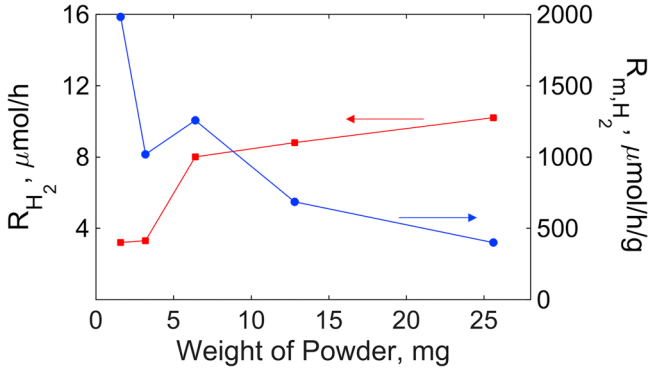

Fig. 7. The effect of the weight of the catalyst on the absolute (R_{H_2}) and the mass specific (R_{m,H_2}) rate of hydrogen production for the second run. The absolute rate is denoted by red squares and the scale on the left axis. The mass specific rate is denoted by blue circles and the scale on the right axis.

carriers. Band bending in the core is important because considering the thickness of the anatase TiO_2 shell (50 − 100 nm), the light absorption coefficients for the $BaTiO_3$ core ($1 \times 10^5\,cm^{-1}$) [35] and the anatase shell ($1 \times 10^2\,cm^{-1}$) [36] at the photon energy of 3.27 eV, most photons (> 99.9 %) would be absorbed by the $BaTiO_3$ core. Therefore, the majority of the charge carriers will be generated in the $BaTiO_3$ core and transported to the shell. The pH affects the performance of these catalysts through its effect on surface charge and band bending. Because holes are the minority carriers, it is typically assumed that the oxidation half reaction is rate limiting [37]. Simulations have shown that increasing the negative surface charge (higher pH) increases the upward band bending [18]. While this band bending reduces the rate of the photocathodic reaction, it promotes the photoanodic reaction and thus increases the overall rate of reaction. As the potential increases, the overall reaction rate continues to increase until the photocathodic and the photoanodic reaction rates are equal; at greater potentials the photocathodic reaction becomes limiting and the overall reaction rate decreases. These predicted trends agree with the data in Fig. 6 where the hydrogen production rate increases with pH, reaches a maximum at pH 9, and then decreases again to a minimum at pH 11. Note that the unsupported catalyst is not expected to follow this trend because the smaller particles do not support significant band bending [38].

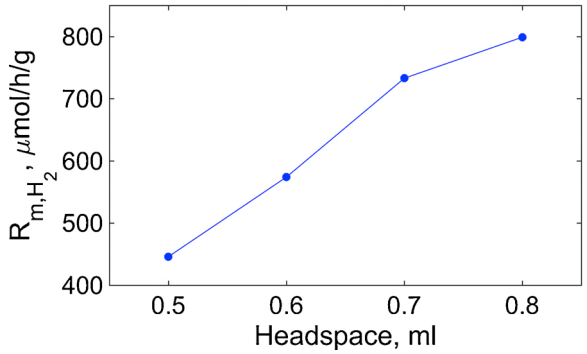

Fig. 8. The mass specific rate of hydrogen production for different volumes of reactor headspace.

The data at pH 2 and pH 12, where there is a large increase in the amount of hydrogen produced, are not consistent with the changes expected as a consequence of differences in surface charge with pH. Note that the reactivity of the core/shell catalyst is consistent with the shell only catalysts, so the maxima at 2 and 12 are not determined by the core/shell structure, but by something happening with the titania or Pt. The sudden increase in the reactivity at pH 12 may be related to a change in the mechanism of oxidation of the methanol. An important step of methanol oxidation is the formation of formaldehyde from $^{\cdot}CH_2OH$. In this step, H^+ is produced and electrons are injected to Pt [34,39]. Therefore, the trapping of electrons on Pt increases when pH increases. The overall reaction rate is thus improved because the photocathodic reaction rate is increased by the availability of electrons in the Pt. The sudden increase in reactivity at pH 2 might similarly be related to a change in mechanism, but the source of this increase is not currently clear.

The core/shell catalyst annealed at 600 °C had measurable hydrogen yields at all pHs, even at pHs where the other catalysts did not produce hydrogen above the 5 % limit. This suggests that for these intermediate pH values, the structure of the catalyst is the feature that leads to improved reactivity. As noted above, the majority of light is absorbed in the core and must be transported through the shell. Therefore, the $BaTiO_3$ core acts as a photon absorber and supplies carriers to the coating. The ferroelectric domains in $BaTiO_3$ are thought to separate photogenerated charge carriers and reduce recombination [40,41]. Measurements of very long carrier lifetimes in $BaTiO_3$ support this idea [21] and this is the most likely reason for the relatively greater reactivity of the core-shell catalyst at intermediate pH. The superiority of the catalyst annealed at 600 °C compared to those annealed at 500 °C and 700 °C is thought to be related to the structure. As concluded by Li et al. [24], who studied the same catalysts at a single pH near 6, annealing at 600 °C improves the crystallinity of the titania and the quality of the core/shell interface, but annealing above this temperature leads to a dramatic reduction in the surface area and reactivity.

It is interesting to note that the performance of the core/shell catalyst is related to the size of the core. The catalysts labeled "5" and "nB" are both $BaTiO_3$ cores coated with titania and annealed at 500 °C. The one difference is that the catalyst labeled “nB” had 100 nm diameter cores and the catalyst labeled “5” had cores at least ten times larger. The relatively poorer performance of the catalysts with nanosized cores can be ascribed to difference in the space charge regions in the $BaTiO_3$ core. The width of the space charge region was calculated to be ≈100 nm [42], which is comparable to the particle size of the nano-size $BaTiO_3$, and thus the potential drop within the space charge region was not as great as in the larger cores.

The PAPCR multi-reactor array used in current work produced results that were qualitatively similar to results for the same catalysts measured in conventional gas-tight reactor system [24,32]. However, there were two main differences. The first difference was that the conventional gas-tight reactor system showed neither an initial “incubation” period nor a final saturation regime; the relation between hydrogen yield and time was approximately linear. One reason for this is that the gas-tight reactor was evacuated before irradiation. This was not possible in the PAPCR, so the pre-existing pressure in our reactors suppressed hydrogen generation from the beginning, creating the incubation period. In addition, the conventional reactor had 25 % more headspace and half the catalyst-to-liquid ratio. Both of these factors contribute to a more rapid pressure increase that suppresses the reaction and leads to the final saturation regime. The second difference between the PAPCR results and the results from the conventional reactor is the difference in the absolute magnitude of the mass specific rate of hydrogen production (which was higher for the PAPCR measurements). This difference is not at all surprising considering that different illumination sources, with different spectral characteristics and illumination geometries, were used. The current work uses light from two 100 W UV LEDs with an emission spectrum narrowly distributed about 380 nm that enters the reactor only through the bottom of the vial. The conventional reactor used a 57 W medium pressure Hg immersion lamp with emission in the range of 280 – 388 nm.

The observation of the saturation regime near the end of the experiment is best explained by the pressure build-up in the reactor. One might speculate that this is a result of catalyst degradation or deactivation. However, the fact that the hydrogen yield versus time can be reproduced after venting the reactors shows that the catalyst has not lost activity. From the same observation, one can also see that the loss of activity is not a result of exhaustion of the hole scavenger, methanol. This is supported by the fact that based on the amount of hydrogen produced, only ≈1 % of the methanol is consumed by the reaction and that the reaction rate is not strongly sensitive to the methanol concentration. Further evidence for the conclusion that pressure build-up causes the saturation is provided by the observation that the mass specific rate of hydrogen production increases with headspace, as indicated in Fig. 8. The additional headspace reduces the rate of pressure build-up. Finally, it is worth noting that the logarithmic behavior that results from the pressure build-up model is consistent with the shape of the hydrogen production versus time data.

It is noted that oxygen remained in the headspace and the solution, which might lead to concerns regarding the back reaction of hydrogen with oxygen on platinum. However, the amount of dissolved oxygen was only ~0.1 μmol [43] and the adsorption of oxygen on platinum is negligible without any external bias [44]. Therefore, this back reaction should not be a significant factor that affects the amount of hydrogen detected.

While the response of the PAPCR is not the same as the conventional reactor, the results derived from it are consistent with prior studies of the same catalysts [24]. The significant advantage of the PAPCR is that up to 96 different catalysts (in the current design) can be tested in the same amount of time as one catalyst in a conventional reactor. This makes it possible to systematically test catalysts prepared in different ways and develop structure-property relationships. For example, the current study showed the effects of core size and annealing temperature on hydrogen production for a $BaTiO_3/TiO_2$ core/shell catalyst at a range of pHs. Using the PAPCR to collect large amounts of data may also enable the application of machine learning to identify and engineer more efficient photocatalysts.

5. Conclusions

The effect of pH on hydrogen production from four kinds of $BaTiO_3/TiO_2$ core/shell catalysts and their components was measured in a highly parallel experiment. The results from the PAPCR are consistent with results from a conventional reactor at a single pH. The core/shell photocatalysts annealed at 600 °C showed the most interesting pH effect. Within the pH range 3–9, the changes in the rate of hydrogen production with pH were ascribed to the effect of pH on surface

potential. At high pH, more negative charge is adsorbed on the surface and this draws more holes (the minority carrier) to the surface to oxidize methanol. The transport of electrons becomes rate limiting when pH is greater than 9, until pH 12, where the injection of electrons into Pt leads to the maximum reactivity. The results show that hydrogen yield from core/shell catalysts is sensitive to both pH and the exact catalyst structure and that these effects can be studied efficiently using a parallel photochemical reactor.

CRediT authorship contribution statement

Wenjia Song: Investigation, Data curation, Formal analysis, Writing - original draft. **Eric M. Lopato:** Investigation, Data curation, Formal analysis. **Stefan Bernhard:** Conceptualization, Methodology, Supervision, Writing - review & editing. **Paul A. Salvador:** Conceptualization, Supervision, Writing - review & editing. **Gregory S. Rohrer:** Conceptualization, Supervision, Funding acquisition, Project administration, Resources, Writing - review & editing.

Declaration of Competing Interest

The authors declare that they have no known competing financial interests or personal relationships that could have appeared to influence the work reported in this paper.

Acknowledgements

This work was supported by the National Science Foundation (DMR 1609369 and CHE 1764353). W.S., P.A.S., and G.S.R. acknowledge the use of the Materials Characterization Facility at Carnegie Mellon University supported by grant MCF-677785. Seed funding for the development of the high-throughput reactors came from CMU's Kavcic-Moura Fund and Manufacturing Futures Initiative. E.M.L. was supported by the Steinbrenner Institute Graduate Fellowship.

Appendix A. Supplementary data

Supplementary material related to this article can be found, in the online version, at doi:https://doi.org/10.1016/j.apcatb.2020.118750.

References

[1] F.E. Osterloh, Inorganic materials as catalysts for photochemical splitting of water, Chem. Mater. 20 (2008) 35–54, https://doi.org/10.1021/cm7024203.
[2] S. Chen, T. Takata, K. Domen, Particulate photocatalysts for overall water splitting, Nat. Rev. Mater. 2 (2017) 17050, , https://doi.org/10.1038/natrevmats.2017.50.
[3] K. Takanabe, Photocatalytic water splitting: quantitative approaches toward photocatalyst by design, ACS Catal. 7 (2017) 8006–8022, https://doi.org/10.1021/acscatal.7b02662.
[4] Y. Ni, H. Zheng, N. Xiang, K. Yuan, J. Hong, Simple hydrothermal synthesis and photocatalytic performance of coral-like $BaTiO_3$ nanostructures, RSC Adv. 5 (2015) 7245–7252, https://doi.org/10.1039/c4ra13642j.
[5] W. Song, P.A. Salvador, G.S. Rohrer, The effect of pH on the photochemical reactivity of $BaTiO_3$, Surf. Sci. 675 (2018) 83–90, https://doi.org/10.1016/j.susc.2018.04.021.
[6] S. Chakrabarti, B.K. Dutta, Photocatalytic degradation of model textile dyes in wastewater using ZnO as semiconductor catalyst, J. Hazard. Mater. 112 (2004) 269–278, https://doi.org/10.1016/j.jhazmat.2004.05.013.
[7] N. Daneshvar, D. Salari, A.R. Khataee, Photocatalytic degradation of azo dye acid red 14 in water on ZnO as an alternative catalyst to TiO_2, J. Photochem. Photobiol. A 162 (2004) 317–322, https://doi.org/10.1016/S1010-6030(03)00378-2.
[8] Y. Wu, H. Wang, W. Tu, Y. Liu, Y.Z. Tan, X. Yuan, J.W. Chew, Quasi-polymeric construction of stable perovskite-type $LaFeO_3$/g-C_3N_4 heterostructured photocatalyst for improved Z-scheme photocatalytic activity via solid p-n heterojunction interfacial effect, J. Hazard. Mater. 347 (2018) 412–422, https://doi.org/10.1016/J.JHAZMAT.2018.01.025.
[9] M.B. Tahir, M. Sagir, Carbon nanodots and rare metals (RM = La, Gd, Er) doped tungsten oxide nanostructures for photocatalytic dyes degradation and hydrogen production, Sep. Purif. Technol. 209 (2019) 94–102, https://doi.org/10.1016/J.SEPPUR.2018.07.029.
[10] R. Asahi, T. Morikawa, T. Ohwaki, K. Aoki, Y. Taga, Visible-light photocatalysis in nitrogen-doped titanium oxides, Science 293 (2001) 269–271, https://doi.org/10.1126/science.1061051.
[11] J. Fu, B. Zhu, C. Jiang, B. Cheng, W. You, J. Yu, Hierarchical porous O-doped g-C_3N_4 with enhanced photocatalytic CO_2 reduction activity, Small 13 (2017) 1603938, , https://doi.org/10.1002/smll.201603938.
[12] R. Shi, H.-F. Ye, F. Liang, Z. Wang, K. Li, Y. Weng, Z. Lin, W.-F. Fu, C.-M. Che, Y. Chen, Interstitial P-doped CdS with long-lived photogenerated electrons for photocatalytic water splitting without sacrificial agents, Adv. Mater. 30 (2018) 1705941, , https://doi.org/10.1002/adma.201705941.
[13] Q. Zhang, D.Q. Lima, I. Lee, F. Zaera, M. Chi, Y. Yin, A highly active titanium dioxide based visible-light photocatalyst with nonmetal doping and plasmonic metal decoration, Angew. Chem. 123 (2011) 7226–7230, https://doi.org/10.1002/anie.201101969.
[14] H. Zhang, L. Zhao, F. Geng, L.-H. Guo, B. Wan, Y. Yang, Carbon dots decorated graphitic carbon nitride as an efficient metal-free photocatalyst for phenol degradation, Appl. Catal. B 180 (2016) 656–662, https://doi.org/10.1016/j.apcatb.2015.06.056.
[15] Z. Pan, Y. Zheng, F. Guo, P. Niu, X. Wang, Decorating CoP and Pt nanoparticles on graphitic carbon nitride nanosheets to promote overall water splitting by conjugated polymers, ChemSusChem 10 (2017) 87–90, https://doi.org/10.1002/cssc.201600850.
[16] R.-A. Doong, C.-H. Chen, R.A. Maithreepala, S.-M. Chang, The influence of pH and cadmium sulfide on the photocatalytic degradation of 2-chlorophenol in titanium dioxide suspensions, Water Res. 35 (2001) 2873–2880, https://doi.org/10.1016/S0043-1354(00)00580-7.
[17] X. Zhu, S.R. Castleberry, M.A. Nanny, E.C. Butler, Effects of pH and catalyst concentration on photocatalytic oxidation of aqueous ammonia and nitrite in titanium dioxide suspensions, Environ. Sci. Technol. 39 (2005) 3784–3791, https://doi.org/10.1021/es0485715.
[18] J.J. Glickstein, P.A. Salvador, G.S. Rohrer, Computational model of domain-specific reactivity on coated ferroelectric photocatalysts, J. Phys. Chem. C. 120 (2016) 12673–12684, https://doi.org/10.1021/acs.jpcc.6b03875.
[19] J.L. Giocondi, G.S. Rohrer, Spatially selective photochemical reduction of silver on the surface of ferroelectric barium titanate, Chem. Mater. 13 (2001) 241–242, https://doi.org/10.1021/cm000890h.
[20] Y. Cui, J. Briscoe, S. Dunn, Effect of ferroelectricity on solar-light-driven photocatalytic activity of $BaTiO_3$ – influence on the carrier separation and stern layer formation, Chem. Mater. 25 (2013) 4215–4223, https://doi.org/10.1021/cm402092f.
[21] M.R. Morris, S.R. Pendlebury, J. Hong, S. Dunn, J.R. Durrant, Effect of internal electric fields on charge carrier dynamics in a ferroelectric material for solar energy conversion, Adv. Mater. 28 (2016) 7123–7128, https://doi.org/10.1002/adma.201601238.
[22] S.H. Wemple, Polarization fluctuations and the optical-absorption edge in $BaTiO_3$, Phys. Rev. B 2 (1970) 2679–2689, https://doi.org/10.1103/PhysRevB.2.2679.
[23] N.V. Burbure, P.A. Salvador, G.S. Rohrer, Photochemical reactivity of titania films on $BaTiO_3$ substrates: influence of titania phase and orientation, Chem. Mater. 22 (2010) 5831–5837, https://doi.org/10.1021/cm1018019.
[24] L. Li, X. Liu, Y. Zhang, P.A. Salvador, G.S. Rohrer, Heterostructured (Ba,Sr)TiO_3/TiO_2 core/shell photocatalysts: influence of processing and structure on hydrogen production, Int. J. Hydrogen Energy 38 (2013) 6948–6959, https://doi.org/10.1016/j.ijhydene.2013.03.130.
[25] L. Li, Y. Zhang, A.M. Schultz, X. Liu, P.A. Salvador, G.S. Rohrer, Visible light photochemical activity of heterostructured $PbTiO_3$-TiO_2 core-shell particles, Catal. Sci. Technol. 2 (2012) 1945–1952, https://doi.org/10.1039/c2cy20202f.
[26] D. Yue, X. Qian, Z. Zhang, M. Kan, M. Ren, Y. Zhao, CdTe/CdS core/shell quantum dots cocatalyzed by sulfur tolerant $[Mo_3S_{13}]^{2-}$ nanoclusters for efficient visible-light-driven hydrogen evolution, ACS Sustain. Chem. Eng. 4 (2016) 6653–6658, https://doi.org/10.1021/acssuschemeng.6b01520.
[27] C. Pan, J. Xu, Y. Wang, D. Li, Y. Zhu, Dramatic activity of C_3N_4/$BiPO_4$ photocatalyst with core/shell structure formed by self-assembly, Adv. Funct. Mater. 22 (2012) 1518–1524, https://doi.org/10.1002/adfm.201102306.
[28] K. Maeda, K. Teramura, D. Lu, T. Takata, N. Saito, Y. Inoue, K. Domen, Photocatalyst releasing hydrogen from water, Nature 440 (2006) 295, https://doi.org/10.1038/440295a.
[29] Q. Wang, T. Hisatomi, Q. Jia, H. Tokudome, M. Zhong, C. Wang, Z. Pan, T. Takata, M. Nakabayashi, N. Shibata, Y. Li, I.D. Sharp, A. Kudo, T. Yamada, K. Domen, Scalable water splitting on particulate photocatalyst sheets with a solar-to-hydrogen energy conversion efficiency exceeding 1%, Nat. Mater. 15 (2016) 611–615, https://doi.org/10.1038/nmat4589.
[30] X. Chen, S. Shen, L. Guo, S.S. Mao, Semiconductor-based photocatalytic hydrogen generation, Chem. Rev. 110 (2010) 6503–6570, https://doi.org/10.1021/cr1001645.
[31] E.M. Lopato, E.A. Eikey, Z.C. Simon, S. Back, K. Tran, J. Lewis, J.F. Kowalewski, J. R. Kitchin, Z.W. Ulissi, J. Millstone, S. Yazdi, S. Bernhard, Unpublished results, n.d.
[32] L. Li, G.S. Rohrer, P.A. Salvador, Heterostructured ceramic powders for photocatalytic hydrogen production: nanostructured TiO_2 shells surrounding microcrystalline (Ba,Sr)TiO_3 cores, J. Am. Ceram. Soc. 95 (2012) 1414–1420, https://doi.org/10.1111/j.1551-2916.2012.05076.x.
[33] H. Yi, T. Peng, D. Ke, D. Ke, L. Zan, C. Yan, Photocatalytic H_2 production from methanol aqueous solution over titania nanoparticles with mesostructures, Int. J. Hydrogen Energy 33 (2008) 672–678, https://doi.org/10.1016/J.IJHYDENE.2007.10.034.
[34] T.A. Kandiel, R. Dillert, L. Robben, D.W. Bahnemann, Photonic efficiency and mechanism of photocatalytic molecular hydrogen production over platinized titanium dioxide from aqueous methanol solutions, Catal. Today 161 (2011) 196–201, https://doi.org/10.1016/j.cattod.2010.08.012.
[35] D. Bäuerle, W. Braun, V. Saile, G. Sprüssel, E.E. Koch, Vacuum ultraviolet

reflectivity and band structure of $SrTiO_3$ and $BaTiO_3$, Z. Phys. B. 29 (1978) 179–184, https://doi.org/10.1007/BF01321179.
[36] H. Tang, F. Lévy, H. Berger, P.E. Schmid, Urbach tail of anatase TiO_2, Phys. Rev. B 52 (1995) 7771–7774, https://doi.org/10.1103/PhysRevB.52.7771.
[37] J. Yang, D. Wang, H. Han, C. Li, Roles of cocatalysts in photocatalysis and photoelectrocatalysis, Acc. Chem. Res. 46 (2013) 1900–1909, https://doi.org/10.1021/ar300227e.
[38] W.J. Albery, P.N. Bartlett, The transport and kinetics of photogenerated carriers in colloidal semiconductor electrode particles, J. Electrochem. Soc. 131 (1984) 315–325, https://doi.org/10.1149/1.2115568.
[39] T.L. Villarreal, R. Gómez, M. González, P. Salvador, A kinetic model for distinguishing between direct and indirect interfacial hole transfer in the heterogeneous photooxidation of dissolved organics on TiO_2 nanoparticle suspensions, J. Phys. Chem. B 108 (2004) 20278–20290, https://doi.org/10.1021/jp046539r.
[40] M.A. Khan, M.A. Nadeem, H. Idriss, Ferroelectric polarization effect on surface chemistry and photo-catalytic activity: a review, Surf. Sci. Rep. 71 (2016) 1–31, https://doi.org/10.1016/j.surfrep.2016.01.001.
[41] A. Kakekhani, S. Ismail-Beigi, E.I. Altman, Ferroelectrics: a pathway to switchable surface chemistry and catalysis, Surf. Sci. 650 (2016) 302–316, https://doi.org/10.1016/j.susc.2015.10.055.
[42] A. Bhardwaj, N.V. Burbure, A. Gamalski, G.S. Rohrer, Composition dependence of the photochemical reduction of Ag by $Ba_{1-x}Sr_xTiO_3$, Chem. Mater. 22 (2010) 3527–3534, https://doi.org/10.1021/cm100718t.
[43] W. Xing, G. Yin, J. Zhang, Rotating Electrode Methods and Oxygen Reduction Electrocatalysts, Elsevier, Amsterdam, The Netherlands, 2014.
[44] T. Biegler, R. Woods, Limiting oxygen coverage on smooth platinum anodes in acid solution, J. Electroanal. Chem. Interfacial Electrochem. 20 (1969) 73–78, https://doi.org/10.1016/S0022-0728(69)80008-2.

Supporting Information for

"High-throughput measurement of the influence of pH on hydrogen production from $BaTiO_3/TiO_2$ core/shell photocatalysts"

Wenjia Song,[1] Eric M. Lopato,[2] Stefan Bernhard,[2] Paul A. Salvador,[1] and Gregory S. Rohrer[1]*

[1]Department of Materials Science and Engineering, Carnegie Mellon University, Pittsburgh, Pennsylvania 15213, United States

[2]Department of Chemistry, Carnegie Mellon University, Pittsburgh, Pennsylvania 15213, United States

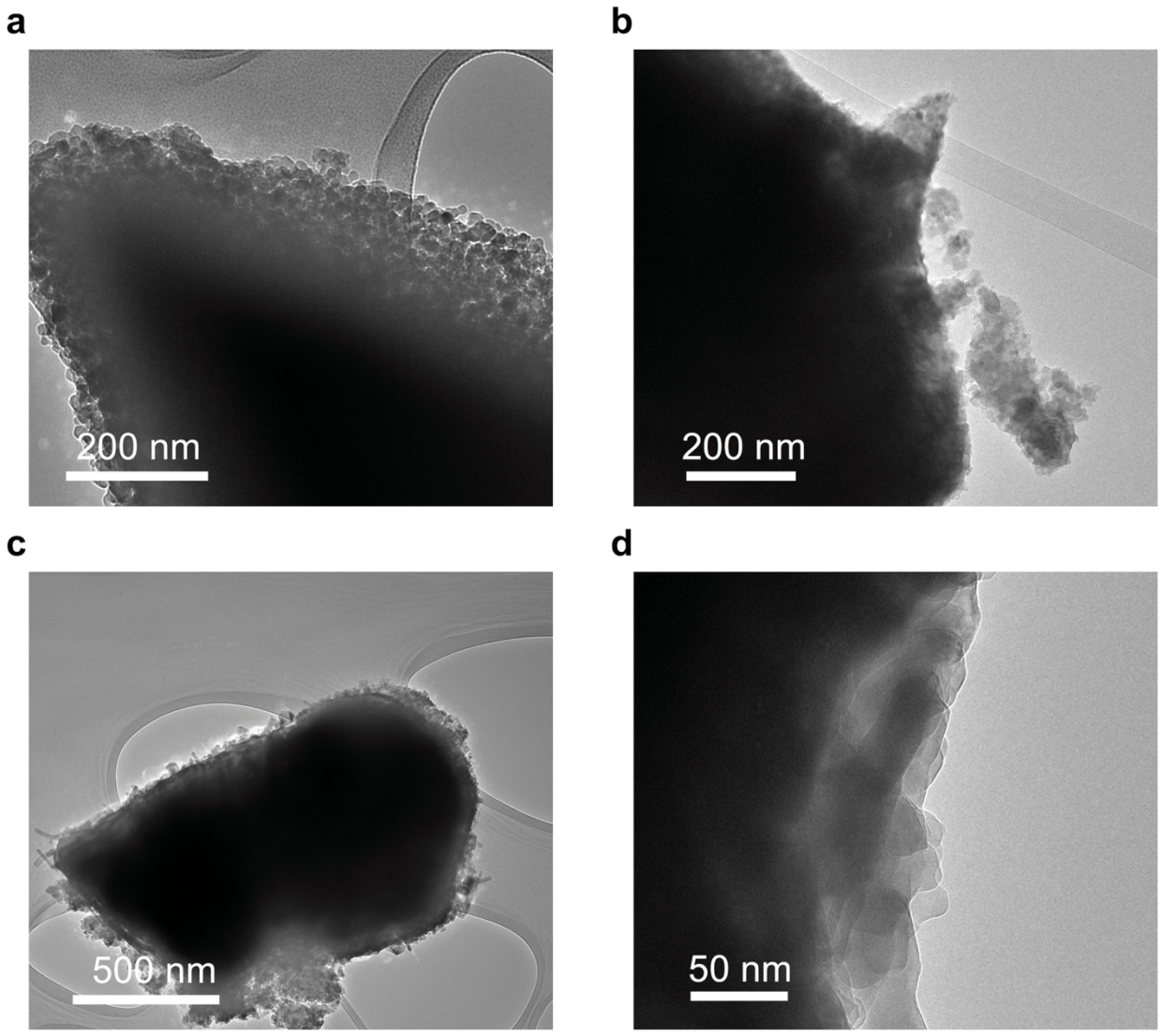

Figure S1. TEM images of the $BaTiO_3/TiO_2$ core/shell powder (annealed at 600 °C after TiO_2 coating).

Hydrogen detection calibration

This new colorimetric chemo-sensitive system was calibrated with known amounts of added hydrogen gas. DetecTape was sealed, with FEP, silicone, and plexiglass, on top of a set of shell vials with holes drilled in the bottom. Custom-made silicone septa, with one side coated in FEP to contain the injected hydrogen, were placed under each vial. Known amounts of atmospheric

pressure hydrogen gas was then inserted through these septa using a gas-tight syringe, and the vials were left to sit for 10 min to allow the tape enough time to provide a reproducible response. Pictures were then taken of the tape and RGB values were extracted for a set of pixels in the center of each well. These values were then averaged and divided by the values from the first image taken prior to the addition of hydrogen. The normalized change in intensity was linear with the H_2 concentration and the resulting calibration curve is depicted in Figure S2. This calibration was then used to evaluate the percent hydrogen produced in the parallel photoreactions.

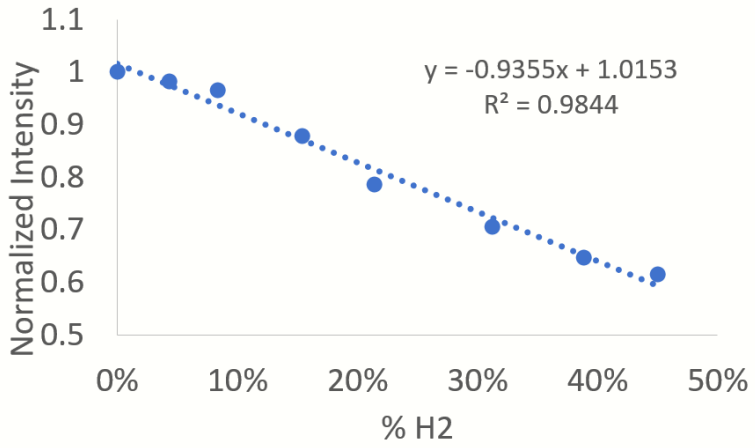

Figure S2. Calibration curve for the tape in the photoreactor presented as intensity normalized to intensity without added hydrogen. Percent hydrogen is shown as partial pressure to the total pressure present. Each point is an average of the values taken from various wells placed across the 96 wells.

The derivation of the logarithmic relationship

According to the theory of pressure effects on reaction rates,[1]

$$lnk = lnk_0 - \frac{\Delta\, ^{\ddagger}V^0}{RT}P \qquad (1)$$

where k is the rate constant at pressure P; k_0 is the rate constant at zero pressure; $\Delta\ ^{\ddagger}V^0$ is the volume change in going from the initial state to the activated state, known as the volume of activation; R is the universal gas constant; and T is the temperature. It was assumed that the temperature was constant and the volume of activation was independent of pressure. The overall photochemical reaction in this work was assumed to be:[2]

$$CH_3OH + H_2O \rightarrow 3H_2 + CO_2$$

The rate of this reaction can be defined as:

$$r = \frac{1}{3}\frac{dp_{H_2}}{dt} \tag{2}$$

where p_{H_2} is the partial pressure of hydrogen. Note that the rate of the reaction can be linked to the rate constant as follows:

$$r = k[CH_3OH]^n[H_2O]^m \tag{3}$$

where n and m are the reaction orders, and $[CH_3OH]$ and $[H_2O]$ are the concentrations of methanol and water, respectively. Based on the highest calibrated limit for the amount of hydrogen (28.6 μmol), the consumption of methanol and water in a typical reaction were only ~ 1 % of the initial volume. Therefore, the concentrations of methanol and water were assumed to be constant. Using Equations 2 and 3, we may express the rate constant as:

$$k = \frac{1}{3}\frac{dp_{H_2}}{dt}\frac{1}{[CH_3OH]^n[H_2O]^m} \tag{4}$$

The other variable in Equation 1, the pressure P, was estimated to be:

$$P = P_0 + p_{H_2} \tag{5}$$

where P_0 is atmospheric pressure. This expression assumes that the change in pressure was only because of the production of hydrogen. This was based on the fact that the solubility of H_2 is lower than the minimum calibrated amount.[3] The pressure change due to the generation of CO_2 was not

included because it is proportional to p_{H_2}; this would only add a constant coefficient to p_{H_2} in Equation 5. This treatment also shows that the logarithmic form of the pressure effect will not be influenced by the actual components of the final product, including gaseous (CO_2) or non-gaseous (formaldehyde or formic acid) products. Equation 1 can be solved using Equations 4 and 5. The solution takes the form of $y = a + blnx$, where y is the hydrogen production and x is the reaction time. The parameters *a* and *b* are:

$$a = \frac{V}{\Delta\, ^{\ddagger}V^0} ln\left(\frac{\Delta\, ^{\ddagger}V^0}{RT} e^{lnk_0 - \frac{\Delta\, ^{\ddagger}V^0}{RT}P_0 + ln(3[CH_3OH]^n[H_2O]^m)}\right) \quad (6)$$

$$b = \frac{V}{\Delta\, ^{\ddagger}V^0} \quad (7)$$

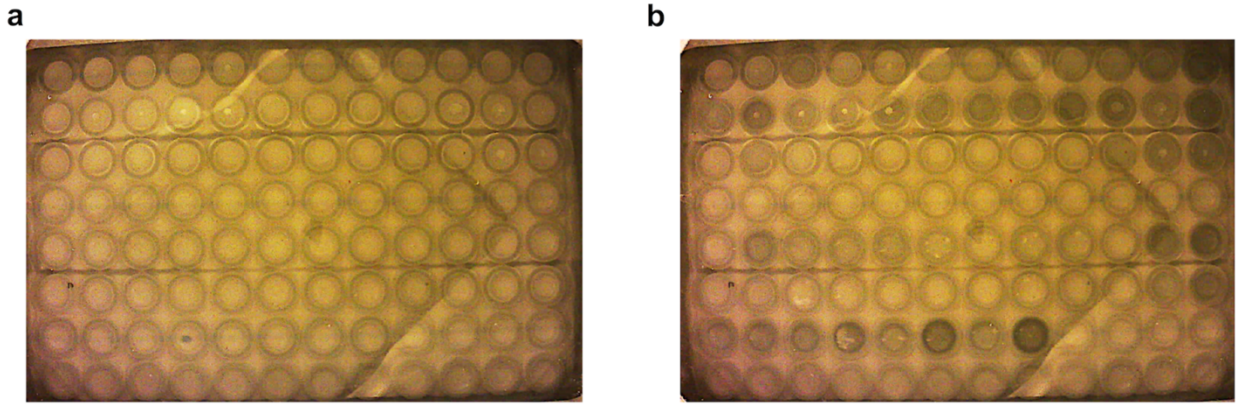

Figure S3. The pictures taken above the reactor array at time (a) t = 0 and (b) t = 6 h. The diagonal lines are the results of refraction at the interface between the tape and the silicone plate. The two horizontal lines below the 2nd row and the 5th row are the edges of the hydrogen sensitive film. The film was three rows wide and three of them were used to cover the entire reactor array. The brightness, contrast, and the sharpness of the pictures shown above have been adjusted for better presentation, while the hydrogen yield data was extracted from raw images.

Extra data processing for the first run

In Figure S4, there is a downward discontinuity at ~ 4 h in the plot for every reactor. This resulted from an abrupt change in the overall brightness of the digital image caused by an instability in the camera or light source. To ameliorate the effect of this artifact, the data from the first 4 h and the last 2 h were processed separately using the method described in the experimental methods section. The separate processing of the different time periods led to two different maximum observable rates of hydrogen production; the larger of the two were defined as the maximum observable rate for this reactor. The data points within the time period having the maximum rate was also used to calculate the incubation time, and parameters *a* and *b*. This discontinuity was not observed in the second run, and thus the extra processing was not needed.

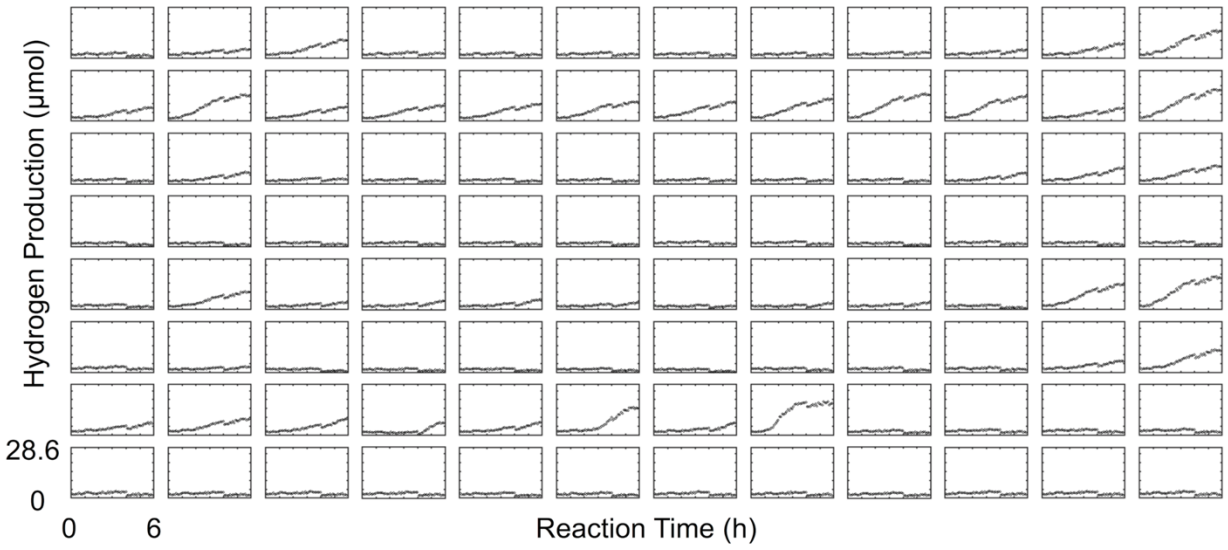

Figure S4. The hydrogen production as a function of reaction time for each reactor in the array. The ranges of the x-axis (0 to 6 h) and the y-axis (0 to 28.6 µmol) are the same for all subplots.

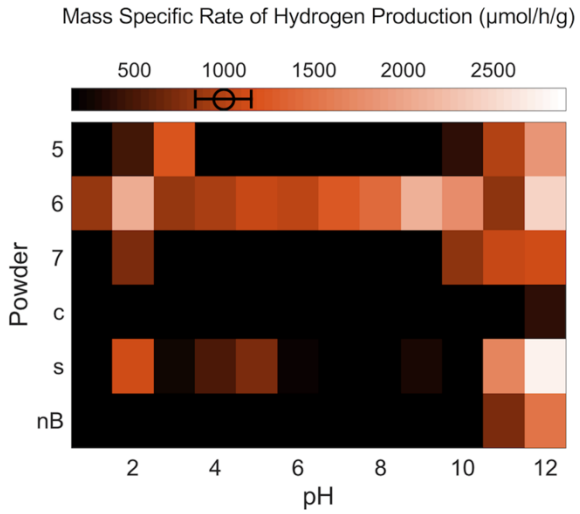

Figure S5. Mass specific rate of hydrogen production of suspensions with six types of powders under different pH conditions shown on a heat map. The average value and the standard deviation calculated from five vials containing identical suspensions are depicted in the color scale bar. The bar is twice the standard deviation.

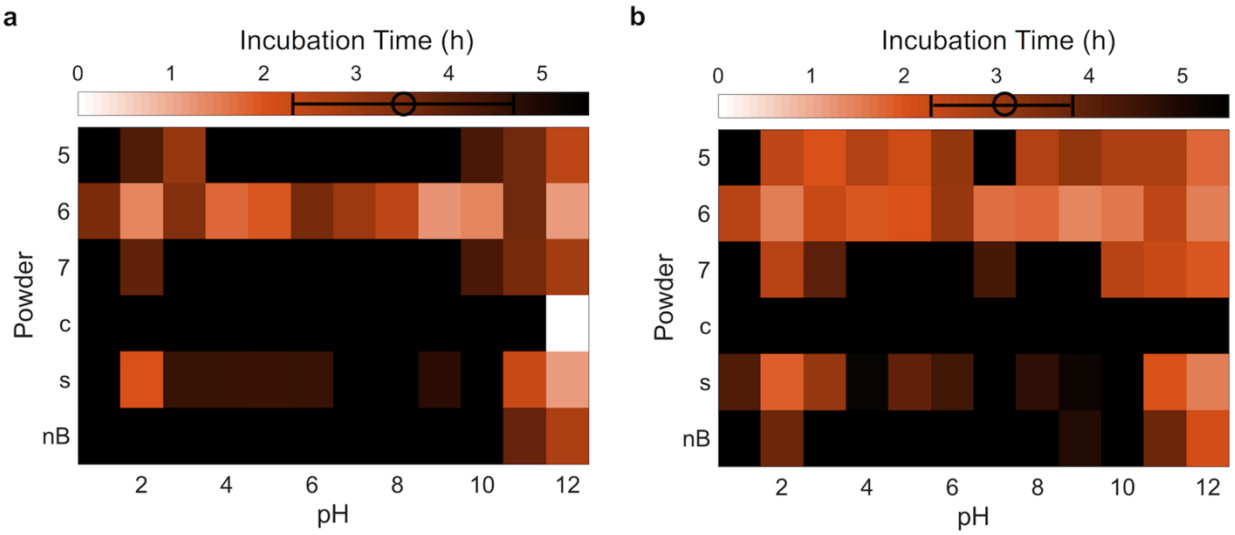

Figure S6. Color visualization of the incubation time of suspensions with six types of powders under different pH conditions for (a) the first and (b) the second run. The average value and the standard deviation calculated from five vials containing identical suspensions are depicted in the

color scale bar. The error bar is twice the standard deviation. Note that in comparison to Fig. S5, the color scale has been reversed.

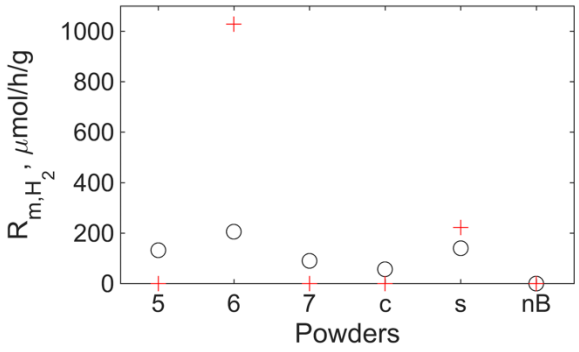

Figure S7. Comparison between the mass specific rates (R_{m,H_2}) of hydrogen production for catalysts synthesized using similar methods yet measured using different methods. The red crosses denote results obtained from PAPCR method (the second run) and the black circles from conventional method (results from ref 4)[4]. Note that the results below the 5% limit are plotted as 0 for the PAPCR method.

Explanations for the parameters *a* and *b*

The parameters a and b in $y = a + blnx$ were also obtained for both runs and are presented in Figure S8 and Figure S9. The parameter a, which is the y-intercept of $y = a + blnx$, would be zero in the ideal case. However, because of the variable incubation period, during which the minimal detectible amount of hydrogen is formed, it takes non-zero values. As illustrated in Figure S8a and Figure S9a, there is considerable scatter in a; the standard deviation in a is ~ 63 % of the average a for both reactions. Because there are no valid data to fit in this time domain, the amount of scatter is not surprising. The parameter b is expected to be a constant. As shown in Figure S8b and Figure S9b, the standard deviation is ~ 29 % of the average value. This range of uncertainty is similar to that of the rate and the incubation time.

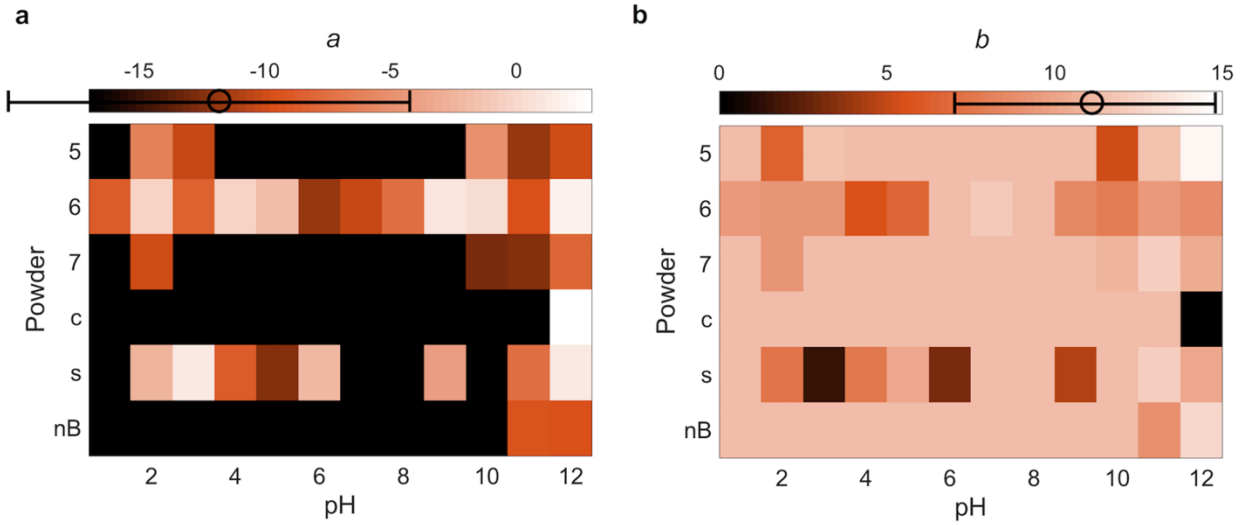

Figure S8. Parameters *a* and *b* of suspensions with six types of powders under different pH conditions for the first run shown on a heat map. The average value and the standard deviation calculated from five vials containing identical suspensions are depicted in the color scale bar. The error bar is twice the standard deviation.

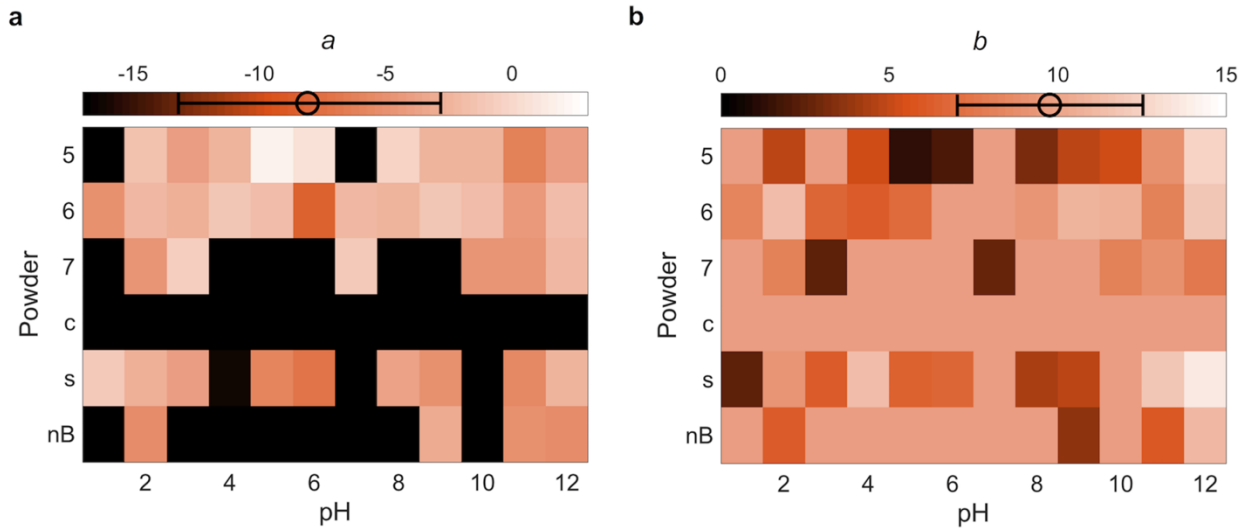

Figure S9. Parameters *a* and *b* of suspensions with six types of powders under different pH conditions for the second run shown on a heat map. The average value and the standard deviation calculated from five vials containing identical suspensions are depicted in the color scale bar. The error bar is twice the standard deviation.

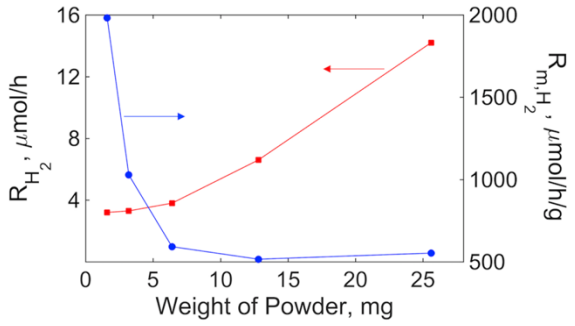

Figure S10. The effect of the weight of the catalyst on the absolute (R_{H_2}) and the mass specific (R_{m,H_2}) rate of hydrogen production. The absolute rate is denoted by red squares and the scale on the left axis. The mass specific rate is denoted by blue circles and the scale on the right axis.

References

1 K. J. Laidler and J. H. Meiser, *Physical Chemistry*, Benjamin/Cummings Publishing Company, Menlo Park, CA, 1982.

2 T. L. Villarreal, R. Gómez, M. González and P. Salvador, *J. Phys. Chem. B*, 2004, **108**, 20278–20290.

3 T. E. Crozier and S. Yamamoto, *J. Chem. Eng. Data*, 1974, **19**, 242–244.

4 L. Li, X. Liu, Y. Zhang, P. A. Salvador and G. S. Rohrer, *Int. J. Hydrogen Energy*, 2013, **38**, 6948–6959.